Detection of overtone and combined peaks using Mn/Cu helical star-shaped (pine-tree-like) sculptured thin films in surface-enhanced Raman spectroscopy

Reza Babaei[2] · Shokoofe Goli-Haghighi[1] · Hadi Savaloni[1]

Abstract

Mn helical star-shaped (pine-tree-like) nano-sculptured thin films with three-, four-and fivefold symmetry on copper substrates were produced using oblique angle deposition method in conjunction with rotation of sample holder at certain angles. Raman spectroscopy of the samples which were subjected to impregnation by 4,4′-bipyridine ($C_{10}H_8N_2$) solution was carried out by 632.8 nm wavelength laser. The analysis of the Raman spectra showed enhancement for the 4,4′-bipyridine main bands (1592 and 1297 cm^{-1}) belonging to the C=C stretching mode, aromatic ring stretching ring and in-plane ring mode of 4,4′-bipyridine, same as results obtained for Ag nano-structures. In addition, overtone and combined peaks are detected that may be related to the particular sculptured structure of the thin films fabricated in this work and the laser wavelength used for Raman spectroscopy. UV–Vis (absorption mode) spectra showed consistent observations with the SERS results leading to important role of surface electromagnetic selection rule in intensification of SERS, in addition pointing out the importance of the effect of the size of hot spots on the frequency of the localized surface plasmonic oscillations.

Introduction

Interaction of light with matter has been a subject of interest to scientists for ages. In 1928, Raman reported occurrence of a type of inelastic scattering [1]. In this phenomenon, absorption of an incident photon leads to formation (stocks) or annihilation (anti-stocks) of an oscillation in the matter, and a photon with different energy emitted/scattered from the matter. Study of the energy spectrum of the emitted/scattered photons provides important information about the structure and bounds in the matter. Nondestructive nature of this method and the fact that there is no special sample treatment for it has proved to be a method of high potential in material science. For this reason, there has been a large

amount of efforts in increasing the cross section (probability of occurrence of this phenomenon). In 1974, a research was conducted on pyridine molecules bounded on an Ag electrode which was roughened using electrochemical oxidation–reduction cycle. Results showed intensified Raman peaks [2]. This work became the base for the effect of metallic substrates on the enhancement of Raman peaks. Since then different types of Raman enhancement spectroscopy such as surface-enhanced Raman spectroscopy (SERS) and tip-enhanced Raman spectroscopy (TERS) are reported which have many applications in pharmacy [3–5], medicine [6–13], geology [14–16], forensic investigations [17–20] and many other fields. Theoretical and experimental studies have shown that the reason for intensification of Raman peaks by metallic substrates is formation and resonance of localized surface plasmons on the rough surface of metals [21, 22]. Considering the interesting optical and plasmonic properties of gold, silver and copper metals (noble metals), most of the investigations of enhanced Raman spectroscopy are carried out using this group of metals.

In our earlier work [23], it was shown that departure from use of noble metals in enhanced Raman spectroscopy can

✉ Hadi Savaloni
savaloni@khayam.ut.ac.ir

1 School of Physics, College of Science, University of Tehran, Tehran, Iran

2 Plasma Physics Research Center, Science and Research Branch, Islamic Azad University, Tehran, Iran

be achieved by using Mn nano-sculptured structures as the substrate. Sculptured structures can be designed and fabricated under controlled deposition conditions with sharp tips and recesses with chosen numbers and sizes. Our work [23] showed that the geometry (shape and size) and symmetry of the metal substrate is as important and effective as choosing the metal itself and also cheaper metals such as Mn can produce better results than Au and Ag metals. Hence, they can have high applications in industry and medicine.

On the other hand, in enhanced Raman spectroscopy, combined and overtone levels may also appear which are the results of the interaction of an incident photon with matter leading to two different oscillations which their probability of occurrence in normal Raman is very low [24]. Konde-pati et al. [25] showed that these peaks are as important as the other Raman peaks in diagnosis of primary cancers in human pancreas and colorectal tissue. Hence, their detection can be of high importance in more precise investigation of biological samples.

Our aim in this work was to produce nano-sculptured helical Mn sculptured thin films with pine-tree-like shape and investigate their Raman enhancement factor while they were impregnated with 4,4′-bipyridine molecules (consisting of nitrogen and carbon rings which are bases of many materials used in investigations in pharmacy and medicine). Raman spectroscopy of the samples by a system equipped with a 632.8 nm laser beam resulted in producing not only enhanced basic 4,4′-bipyridine Raman peaks but also showed combined and overtone peaks in the surface-enhanced Raman spectra.

Experimental details

Mn helical star-shaped (pine-tree-like) sculptured thin films (HSSTFs) were deposited on Cu substrates (Goodfellow Metals, Cambridge, UK) ($20 \times 20 \times 1$ mm^3) using electron beam evaporation from a graphite crucible with a diameter of 6 mm at room temperature. The purity of Mn was 99.95% (Goodfellow Metals, Cambridge, UK). An Edwards (Edwards E19 A3) coating vacuum system with a base pressure of 2×10^{-7} mbar was used. The deposition angle was fixed at 80°, and the substrate was rotated clockwise in sudden movements at pre-assigned angles.

The details of substrate holder system are given in our earlier work [26]. A brief description is given here for ease of access for the readers. The movement of the substrate holder is controlled by two stepping motors at two angles α and φ, with 0.01 degree/step accuracy.

An interface to a computer consists of a particular software (written in the LabVIEW format) which controls the speed of rotation of the substrate holder and provides facility for dividing each revolution of the substrate holder to various sections. The substrate holder was a stainless steel disk of 100 mm diameter.

Tait [27] has given the relationship between the axis of columns in the columnar structure and the substrate surface normal "β" for deposition angles "α" larger than 60° as $\beta = \alpha - \sin^{-1}\left(\frac{1-\cos\alpha}{2}\right)$. Hence, for $\alpha = 80°$ a value of $\beta = 55.5°$ was obtained. Therefore, the thickness of each arm with a length of L can be calculated as $L\cos\beta$. The procedure for fabrication of Mn HSSTF5 is as follows:

Stage 1 substrate was fixed in an arbitrary position ($\varphi = 0°$), and 60 nm Mn film was deposited.

Stage 2 substrate was rotated by 180° ($\varphi = 180°$), and at this new position (opposite to Stage 1) 60 nm Mn film was deposited. (First tip point of the star is made in a zigzag shape.)

Stage 3 substrate was rotated by 180° to return to the position of Stage 1 and then rotated by 72°, and 60 nm Mn film was deposited.

Stage 4 substrate was rotated by 180° ($\varphi = 180°$), and at this new position (opposite to Stage 3) 60 nm Mn film was deposited. (Second tip point of the star is made in a zigzag shape.)

Stage 5 substrate was rotated by 180° to return to the position of Stage 3 and then rotated by 72°, and 60 nm Mn film was deposited.

Stage 6 substrate was rotated by 180° ($\varphi = 180°$), and at this new position (opposite to Stage 5) 60 nm Mn film was deposited. (Third tip point of the star is made in a zigzag shape.)

Stage 7 substrate was rotated by 180° to return to the position of Stage 5 and then rotated by 72°, and 60 nm Mn film was deposited.

Stage 8 substrate was rotated by 180° ($\varphi = 180°$), and at this new position (opposite to Stage 7) 60 nm Mn film was deposited. (Fourth tip point of the star for SHSTF5 is made in a zigzag shape.)

Stage 9 substrate was rotated by 180° to return to the position of Stage 7 and then rotated by 72°, and 60 nm Mn film was deposited.

Stage 10 substrate was rotated by 180° ($\varphi = 180°$), and at this new position (opposite to Stage 9) 60 nm Mn film was deposited. (Fifth tip point of the star for HSSTF5 is made in a zigzag shape.)

Stage 11 substrate was rotated by 180° to return to the position of Stage 9 and then rotated by 72°.

One pitch of the helical Mn star-shaped structure is completed, and the substrate holder is in the position of Stage 1; Stages 1 to 11 may be repeated for fabrication of second and third pitches of the Mn HSSTF5.

The second pitch and the third pitch of the sculptured structure were fabricated by repeating the above stages while the lengths of arms were decreased to 30 nm and 15 nm, respectively. Therefore, the final structure should look like a pine tree.

Deposition of Mn HSSTF4 and Mn HSSTF3 samples was carried out as above but the 72° rotation angle was changed to 90° and 120°, respectively. Hence, the number of stages was also reduced accordingly.

A quartz crystal deposition rate and thickness controller (Sigma Instruments, SQM-160, USA) which was positioned close to the substrate holder and at the almost the same azimuthal angle as that of the substrate was employed for obtaining the deposition rate during fabrication of the samples which was fixed at 1.0 Å s^{-1}. The deposition rate was estimated from the film thickness obtained from the FESEM image of the cross section of the film divided by the deposition time.

The distance between the evaporation crucible (6 mm in diameter) and the substrate was chosen as 30 cm. Hence, the evaporation source can be considered as a point source with a cosine distribution. In this configuration, it may be assumed that vapor has a straight trajectories (i.e., no appreciable scattering due to the large mean free path ($\sim 5 \times 10^4$ cm [28] occurs).

All Cu substrates were ultrasonically cleaned in heated acetone then ethanol before fixing them on the substrate holder.

In order to make sure of the reproducibility of the results, the deposition process was repeated several times and results of different analyses (e.g., XRD, AFM and FESEM) were compared which showed consistent results within the experimental uncertainties. FESEM images were obtained using a Hitachi S-4100 SEM, Japan field emission electron microscope. AFM (Nt-mdt scanning probe microscope, BL022, Russia; with low stress silicon nitride tip of less than 200 Å radius and tip opening of 18°) images provided the surface roughness and the morphology of the produced samples.

SERS measurements were taken on the star-shaped helical Mn nano-structures with three, four and five pointed tips coated with 4,4′-bipyridine ($C_{10}H_8N_2$), whose powder was dissolved in deionized water, and a solution with 4.5 gl^{-1} (2.885×10^{-2} mol l^{-1}) was obtained. In order to achieve a homogenized solution, the solution was passed through a paper filter before being used for coating of the samples. SERS measurements were taken after drying the samples.

The Raman spectroscopy of the samples was carried out using FT Raman 960 spectrometer, Thermo Nicolet, USA; 632.8 nm. For determination of surface plasmons, UV–Vis spectrometer (StellarNet BLACK, Comet concave grating spectrometer) was employed.

Results and discussion

SEM and AFM; nano-structure

The structures of the samples produced for this work are given in our earlier work [23]. However, in order to give the facility of ease of access to these data to the reader, they are repeated here with a brief description. Figure 1 shows the FESEM images of all three types of samples in both x and y directions (axes). The sharp tips and the voids between the nano-structures can vividly observe. The decrease in the length of arm in the growing pitches is also obvious. The cross-sectional image of the film gives a good measure of the film thickness which was found consistent with the predictions that was obtained from calculations considering geometry of the system [29]. In addition, considering that the length of arms from bottom to the top of the sample is reduced in this conical-shaped sculptured structure resulted in reduced diameter of each pitch relative to the underlying pitch (Fig. 1).

In Fig. 2, 2D and 3D, AFM images of the samples fabricated in this work are given. The use of JMicroVision Code on the 2D AFM images provided the information about the film surface roughness, grain size distribution and the void fraction in the produced samples (Table 1).

X-ray diffraction analysis

XRD patterns of the Mn/Cu sculptured thin films fabricated in this work are given in Fig. 3.

Four clear peaks are present in all samples with three-, four- and fivefold symmetry. Two of the peaks may be assigned to the Cu substrate (Cu(220) and Cu(311) (with respect to the JCPDS card No: 00-003-1018)); one peak belongs to Mn(100) (with respect to the JCPDS card No: 00-003-1014), and the forth peak can be assigned to $MnO_2(041)$ (with respect to the JCPDS card No: 00-007-0222).

Surface-enhanced Raman spectroscopy

A spectrometer with 632.8 nm laser wavelengths was used to analyze the samples. In order to perform Raman measurement on the 4,4′-bipyridine solution itself, the homogenized solution was poured in a thin glass vial of 6 mm diameter covered with a cap cover glass.

SERS spectra of Mn star-shaped samples with three, four and five pointed tips coated with 4,4′-bipyridine and 4,4′-bipyridine solution itself are given in Fig. 4.

The ratio of the area under the peak after subtraction of background for the main bands of 4,4′-bipyridine ($C_{10}H_8N_2$)

Fig. 1 FESEM images of the cross sections of the Mn helical star-shaped (pine-tree-like) sculptured thin films with different symmetries; **a** threefold symmetry, **b** fourfold symmetry, **c** fivefold symmetry. Column I) images are taken from the *x*-direction of the sample. Column II) images are taken from the *y*-direction of the sample
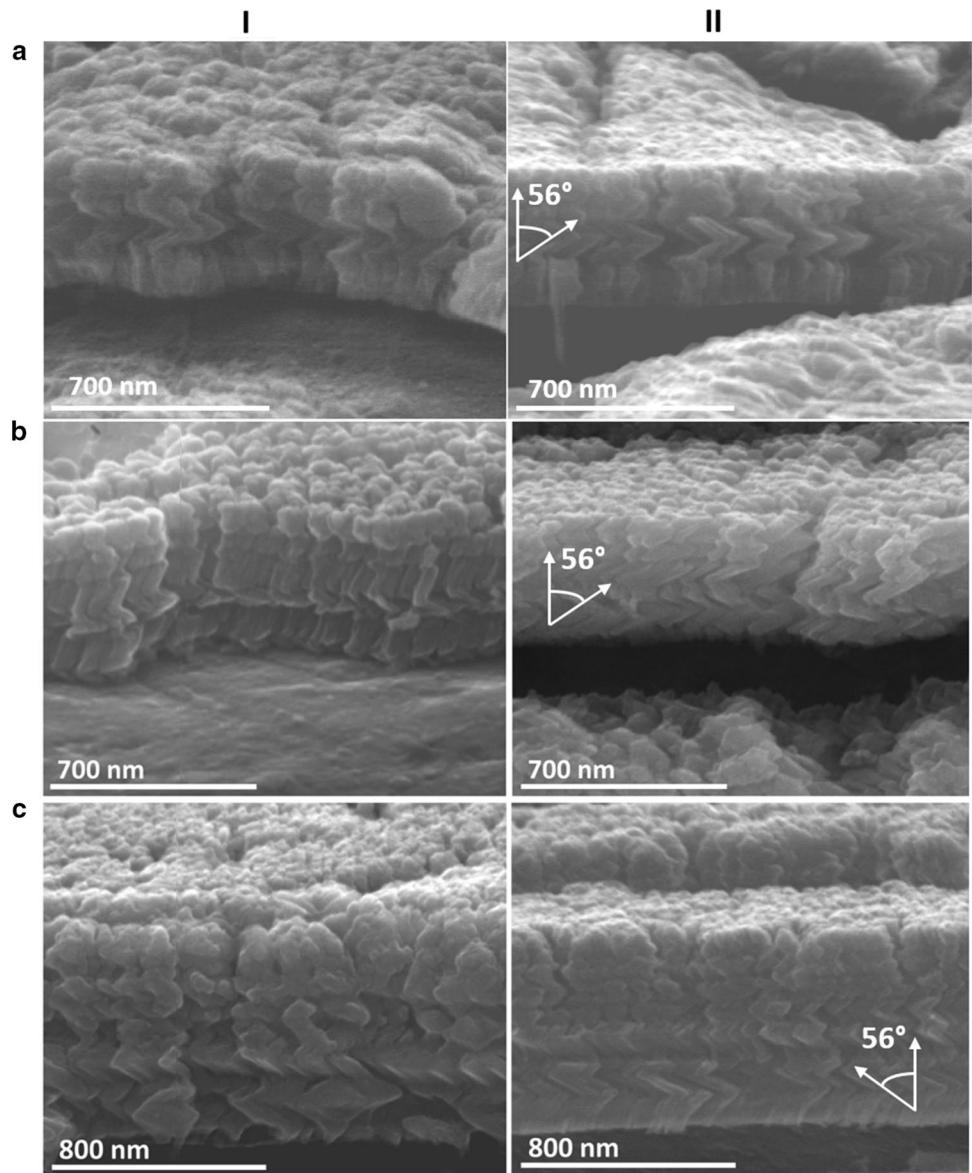
(i.e., 1290, 1410 and 1590 cm^{-1}) to that of 4,4′-bipyridine solution obtained using the 632.8 nm wavelength is given in Table 2. The data in this table show that the threefold symmetry has produced the highest enhancement for these peaks while fivefold symmetry shows slightly less improvement. The fourfold symmetry sample spectrum is even inferior to that of 4,4′-bipyridine solution. The latter could be the result of higher symmetry order of this sample [30].

UV–visible spectra

The absorption spectra of the samples discussed in this work were obtained by a UV–Vis spectrometer (see "Experimental details" section) and are shown in Fig. 5. In these spectra, the shift in the absorption peak position is dependent on the size of particles [31, 32]. The grain size of threefold

symmetry is smaller than fourfold symmetry (Table 1); hence, its absorption peak shows a blue shift relative to that of fourfold symmetry sample, while the grain size of fivefold symmetry sample is larger than that of fourfold symmetry, and its absorption peak shows a red shift relative to that of fourfold symmetry sample.

The UV–Vis spectrum of the Mn sample in Fig. 5 shows no feature/peak while Mn helical star-shaped (pine-tree-like) sculptured samples show peaks at different wavelengths; threefold, fourfold and fivefold symmetry samples have a peak at 632 nm, 720 nm and 786 nm, respectively.

At 632 nm wavelength (Fig. 5), the order of intensity from highest intensity is for fivefold, threefold and fourfold symmetry samples. However, in fact in this type of analysis, one should give more weight to the spectrum
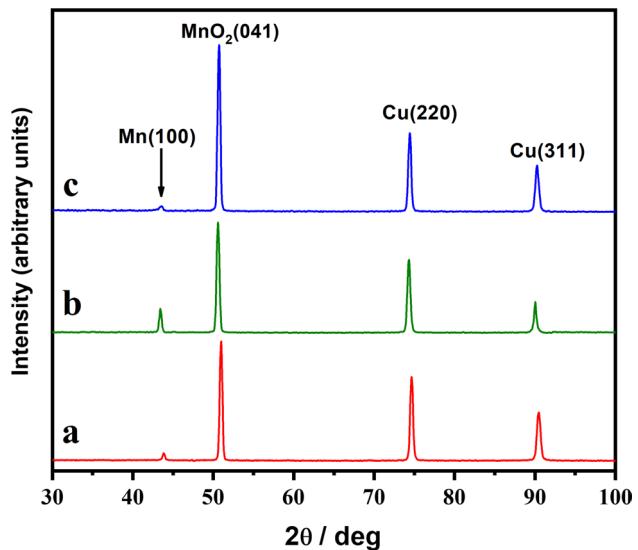
Fig. 2 3D (Column I), 2D (column II) AFM images of the Mn helical star-shaped (pine-tree-like) sculptured thin films with different symmetries; row **a** threefold symmetry, row **b** fourfold symmetry, row **c** fivefold symmetry. Column III) 2D AFM images with gray level used for obtaining surface void fraction of the films
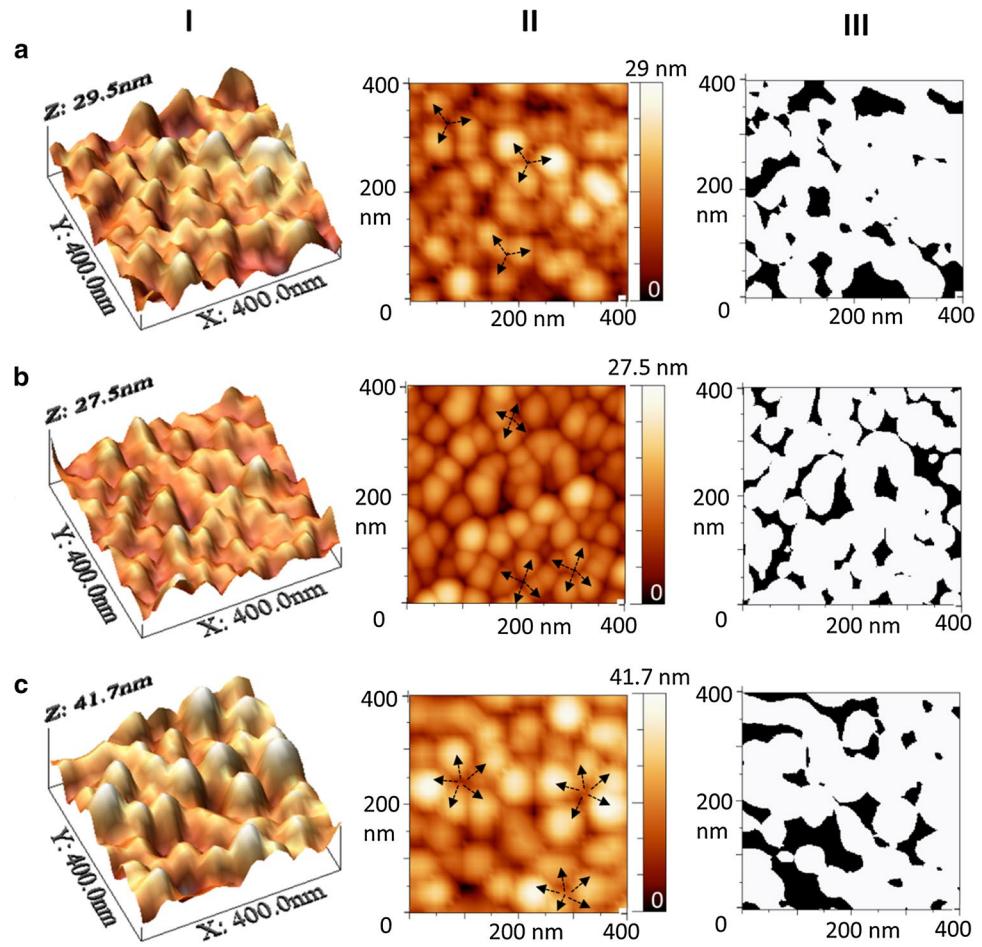
Table 1 Average surface roughness and grain size and surface void fraction of the Mn helical star-shaped (pine-tree-like) sculptured thin films with different symmetries

Mn/Cu star shape	R_{ave} (nm)	R_{rms} (nm)	D_{AFM} (nm)	F_v
Threefold	4.1	5.2	42.3	0.20
Fourfold	3	3.7	48.5	0.18
Fivefold	5.7	7.2	63.3	0.23

consisting of a peak. (Area under the peak should be considered.) Hence, the order will be changed as threefold, fivefold and fourfold which are again consistent with the results of Raman spectra obtained using the Raman spectrometer with 632.8 nm wavelength laser. Therefore, from these agreements between AFM and UV–Vis spectra, it may be concluded that the hot spot size has a direct effect on the position of peak in the absorption spectra (localized surface plasmon frequency). Accordingly, it is logical to accept that the number of hot spots should also directly intensify the Raman peak intensity as they accommodate molecules under investigation.

Fig. 3 XRD patterns of (a) threefold, (b) fourfold and (c) fivefold symmetry Mn helical star-shaped (pine-tree-like) sculptured thin films

Fig. 4 SERS spectra measured using 632.8 nm wavelength laser from (a) 4,4′-bipyridine solution and 4,4′-bipyridine deposited on (b) threefold, (c) fourfold and (d) fivefold symmetry Mn helical star-shaped (pine-tree-like) sculptured thin films
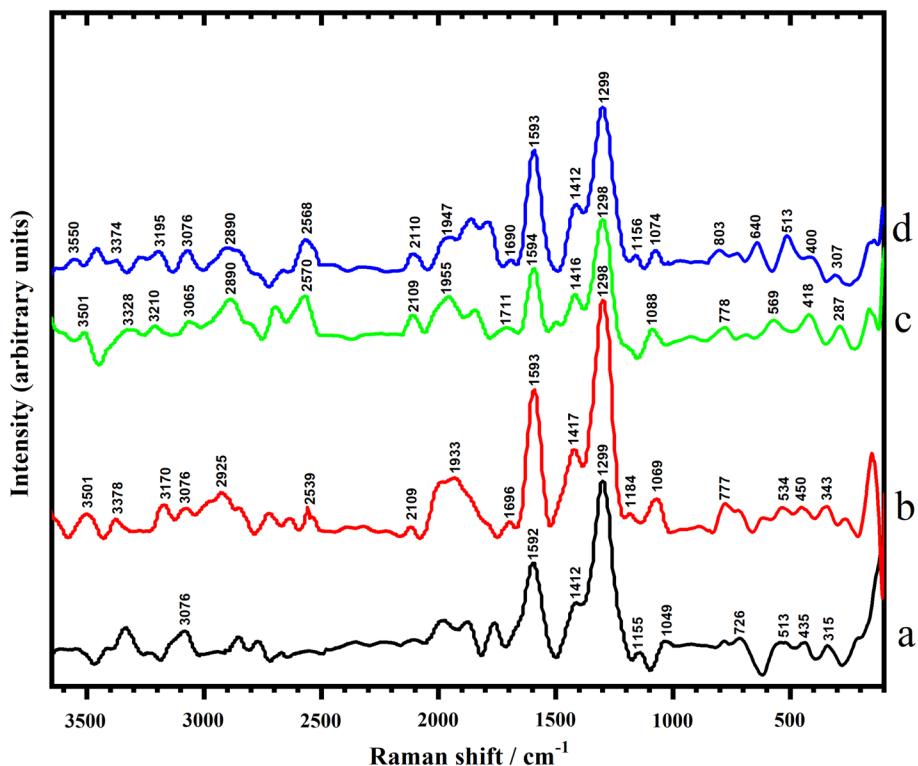
Table 2 Areas under the main peaks of 4,4′-bipyridine deposited on the Mn helical star-shaped (pine-tree-like) sculptured thin films with different symmetries and that of Bipy solution, and their enhancement ratios relative to Bipy solution obtained using 632.8 nm wavelength laser

	$S(1290)$	$S(1410)$	$S(1590)$	$S(1690)$	$S(1947)$	$\frac{S(1290)_{sample}}{S(1290)_{Bipy}}$	$\frac{S(1410)_{sample}}{S(1410)_{Bipy}}$	$\frac{S(1590)_{sample}}{S(1590)_{Bipy}}$
Bipy	66.89	16.44	29.54	–	–	–	–	–
Threefold	89.17	33.87	42.48	0.80	9.10	1.33	2.06	1.44
Fourfold	45.24	13.34	17.06	1.36	3.40	0.68	0.81	0.58
Fivefold	68.86	24.36	35.86	0.28	2.52	1.03	1.48	1.21

Accommodation and orientation of molecules on the surface of the sample

In Fig. 4, it can be seen that only A_g and B_g Raman shifts are present. This is because 4,4′-bipyridine is one of the D_{2h} groups, and according to the gross selection rule for vibrational Raman transitions, vibration of molecule should lead to change in polarizability [33].

In Table 3, the values of Raman shifts obtained from the SERS measurements using 632.8 nm laser for the more pronounced peaks and the corresponding vibrations for the samples discussed in this work are given.

The electromagnetic selection rule [34] suggests that the enhancement of perpendicular mode of vibration is more than parallel mode. The Raman spectra obtained in this work for

different samples are summarized in Table 3. It can be seen that majority of the ring modes belong to in-plane modes, and those belonging to out-of-plane modes are very weak which suggests that the adsorbate is formed in a vertical structure.

Calculation of the enhancement factor

The SERS enhancement factor is calculated using [35];

$$EF = \frac{I}{I_0}\frac{N_0}{N},\qquad(1)$$

where N_0 is the number of 4,4′-bipyridine molecules in the volume of the solution covered with the incident laser beam and N is the number of 4,4′-bipyridine molecules which have the most contribution in SERS (i.e., molecules positioned on the sharp tips (hot spots) of the structure);
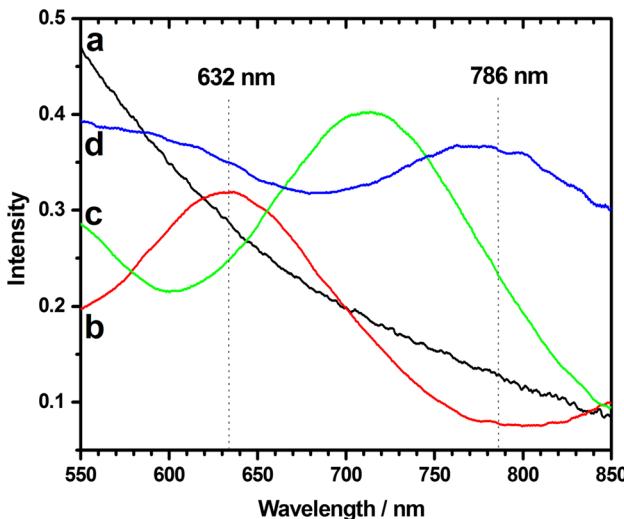
Fig. 5 UV–Vis absorption spectra of (a) Mn substrate and, (b) three-fold, (c) fourfold and (d) fivefold symmetry Mn helical star-shaped (pine-tree-like) sculptured thin films

$$N_0 = 5 \times 10^{-3}\,[\text{m}]\,(\text{Height of solution in vial})$$

$$\times \frac{4.5 \left[\frac{\text{kg}}{\text{m}^3}\right]}{156.8 \left[\frac{\text{kg}}{\text{mole}}\right]} \times 6.022 \times 10^{23}\,[\text{mole}^{-1}]$$

$$\times \text{ cross section of laser beam} \qquad (2)$$

and

$$N = k \times \frac{1.7 \times 10^{-15}\,[\text{m}^2]\,(\text{surface of a spot})}{0.6^2 \times 10^{-18}\,[\text{m}^2]\,(\text{cross section of a Bipy molecule})}$$

$$\times 3 \times n \times 1.1 \times 10^{12} \qquad (3)$$

where n is the symmetry order/fold of the star, k is the coefficient which contains the ratio of number of 4,4′-bipyridine molecules which are positioned in the best orientation for enhancement of the Raman signal to that of the total number of molecules positioned/accommodated on the sharp tip (hot spot). Hence, $n = 3$, 4 and 5 and $0 < k < 1$.

If $k = 1$, then for $n = 3$, 4 or 5 the ratio N_0/N will be 0.75×10^3, 1×10^3 and 1.25×10^3.

Accordingly, the enhancement factor for our samples in this work is of the order of 10^3.

The following assumptions are made in performing these calculations:

Table 3 Spectral data (wave number ($\bar{\nu}_{\text{ScatteredPhoton}}[\text{cm}^{-1}] = \frac{10^7}{\lambda[\text{nm}]}$)) and vibrational assignment of 4,4′-bipyridine (Bipy) solution itself and the Mn helical star-shaped (pine-tree-like) sculptured thin films with different symmetries obtained from measurement with 632.8 nm wavelength laser

Bipy	Threefold	Fourfold	Fivefold	Phonons	$\bar{\nu}_{\text{ScatteredPhoton}}$	Symmetry	Assignment	Remarks
–	3501†	3501†	3550†	1938 and 1590	12,250	–	–	a
–	3378†	3328†	3374†	3070 and 307	12,430	–	–	a
–	3170*	3210*	3195*	2×1597	12,600	A_g	ν_{ring}	–
3076	3076	3065	3076	–	12,727	B_{1g}	ν(CH)	–
–	2925†	2890†	2890†	1300 and 1590	12,900	–	–	a
–	2539†	2570†	2568†	1160 and 1410	13,235	–	–	–
–	2117*	2109*	2110*	2×1097	13,690	B_{1g}	$\nu_{\text{ring}}+\delta$(CH)	–
–	1933†	1955†	1947†	1300 and 638	13,865	–	–	b
–	1696*	1711*	1690*	2×866	14,100	B_{3g}	γ(CH)	–
1592	1593	1594	1593	–	14,210	B_{1g}	ν_{ring}	–
1412	1417	1416	1412	–	14,391	B_{1g}	ν_{ring}	–
1299	1298	1298	1299	–	14,500	A_g	$\nu_{\text{ring}}+\delta$(CH)	–
1155	1184	–	1156	–	14,650	A_g	δ(CH)	–
1049	1069	1088	1074	–	14,730	B_{1g}	$\nu_{\text{ring}}+\delta$(CH)	–
726	777	778	803	–	15,000	A_g	$\nu_{\text{ring}}+\delta$(CH)	c
–	–	–	640*	2×314	15,160	A_g	δ_{ring}	c
513	534	569	513	–	15,290	B_{3g}	γ_{ring}	–

*Overtone peaks, †combined peaks

[a]In threefold: presence of a peak at 15,803 cm^{-1} wave number in the absorption spectrum indicates intensification of incident photon. In fivefold: presence of a peak at 12,500 cm^{-1} wave number in the absorption spectrum indicates intensification of scattered photon

[b]In threefold: presence of a peak at 15,803 cm^{-1} wave number in the absorption spectrum indicates intensification of incident photon. In fourfold: presence of a peak at 14,000 cm^{-1} wave number in the absorption spectrum indicates intensification of scattered photon

[c]In fivefold: presence of a weak peak at 15,160 cm^{-1} wave number in the absorption spectrum indicates intensification of scattered photon

1. The number of stars in unit area of the surface is 1.1×10^{12} which is obtained from the FESEM images of the samples.

2. The value of unity for k indicates the highest concentration of 4,4′-bipyridine molecules on the hot spot which is not a logical probability assumption.

3. The factor 3 in Eq. 3 indicates that all three pitches of the helical structure are considered in the process while penetration of 4,4′-bipyridine molecules to lower pitches is less probable.

However, no considerable change may be resulted from all these in the value of the enhancement factor.

Generally, in the analysis of Raman spectra only the most probable process is considered because of the small intrinsic effective cross section (i.e., the interaction of one photon with one phonon). If a molecule becomes excited by a laser beam at angular frequency ω_k, the linear optical polarizability $\widehat{\alpha}_L$ may be described as a function of the normal mode coordinates $Q_k \left[\text{kg}^{1/2}\text{m} \right]$: $\widehat{\alpha}_L(Q_1, Q_2, \ldots)$ [36].

Hence, a specific normal mode k may be characterized by Q_k where all other $Q_{k'}$ are zero. For internal vibrations are usually small perturbations of the molecular and electronic structure, the polarizability is expected to be also weakly perturbed by their presence. Hence, one may approximate the linear optical polarizability by a Taylor expansion as follows [36]:

$$\widehat{\alpha}_L(Q_k) = \widehat{\alpha}_L(0) + \left(\frac{\partial \widehat{\alpha}_L}{\partial Q_k} \right)_{Q_k=0} Q_k + \frac{1}{2} \left(\frac{\partial^2 \widehat{\alpha}_L}{\partial Q_k^2} \right)_{Q_k=0} Q_k^2 + \cdots \tag{4}$$

The second term in the Taylor expansion is related to the variation in polarizability of the matter as a function of Q_k (the normal mode coordinate) which results in Q_k^2 coefficient and leads to scattering of the form $\omega_L \pm 2\omega_k$. (ω_L and ω_k are corresponding frequencies of the laser and the normal mode k, respectively.) This will cause appearance of peaks with double (twice) Raman shift and called overtones. In addition, it is also possible that two different phonons are produced by absorption of one photon (terms with coefficient of the form $Q_k Q_{k'}$ in the Taylor expansion). Frequency of the scattered photon in this process is $\omega_L \pm (\omega_k \pm \omega_{k'})$ and is called combination band or higher-order scattering. In normal condition, influence of vibrations on the polarizability is considered in form of perturbation and overtones and combination bands are much weaker than the normal Raman phenomenon and cannot be detected unless certain special resonance conditions are met [36].

In this work, in addition to 4,4′-bipyridine characteristic peaks, overtone peaks and combination bands are also observed. In Table 3, the peaks related to the 632.8 nm laser wavelength with their assignments are given.

The Raman spectrum is usually drawn as a function of Raman shifts (wave number of the produced phonon) $\nabla\bar{\nu} \left[\text{cm}^{-1} \right]$. The energy relationship for the Raman phenomenon is as follows:

$$E_{\text{phonon}} = E_{\text{photon(laser)}} - E_{\text{scattered(photon)}} \tag{5}$$

Hence, the relationship between the wave numbers of incident photon and scattered phonon(s) is as follows:

$$\nabla\bar{\nu}_{\text{phonon}} = \bar{\nu}_{\text{photon(laser)}} - \bar{\nu}_{\text{scattered(photon)}} \tag{6}$$

As an example from Table 3, the peak at 3370 may be assumed/accepted as a combination band as a result of summation of a peak at 307 and a peak at 3070. (Both peaks are of main 4,4′-bipyridine characteristic peaks.) Hence, absorption of one photon of the laser light with 632.8 nm wavelength (wave number of 15,802.8 cm^{-1}) in the matter leads to simultaneous production of two phonons with 307 cm^{-1} and 3070 cm^{-1} wave numbers. The wave number relationship of these two wave numbers is 15,802.8–(307 + 3070) = 12,425.8 cm^{-1} which is the wave number of the scattered photon. In the UV–Vis spectra of the samples produced in this work (Fig. 5), it can be observed that the spectrum of the sample with fivefold symmetry has a peak at about 12,500 cm^{-1}. Therefore, we may deduce that the presence of a peak at 3370 cm^{-1} in the Raman spectrum is related to the intensification of photon with 12,426 cm^{-1} wave number that is scattered when two phonons with 307 cm^{-1} and 3070 cm^{-1} wave numbers are simultaneously produced. It should also be mentioned that this peak is also present in the spectrum of threefold symmetry sample with relative strength.

Conclusions

Szabo et al. [37] reported the enhancement of Raman signal from Mn small isolated metal spheres. Hence, in this work Mn was chosen as the material and fabricated nano-sculptured pine-tree-like structures with different symmetries on Cu substrates. Then, SERS investigation was carried out 4,4′-bipyridine molecules embedded on these structures. Results not only showed that the enhancement factor obtained from this work is comparable to that obtained from Ag nano-structures [38, 39], but also lead to detection of overtone and combined peaks of 4,4′-bipyridine molecules which may be related to the sculptured structure of the thin films fabricated in this work and the wavelength of the laser used. In addition, results of SERS showed good agreement with those obtained from UV–Vis (absorption mode) which points out the important role of electromagnetic model for enhancement of Raman scattering. However,

due to surface oxidation of Mn which may act as a buffer between 4,4′-bipyridine molecules and the Mn atoms, one may also consider the role of charge transfer mechanism in this work. Therefore, one cannot define exactly which of these two mechanisms are more likely to explain the results of this work as also being commented in most of the published literature.

The consistency between results obtained from the UV–visible spectrophotometry and that of AFM analysis indicates that the size of hot spots has a determinant effect on the frequency of the localized surface plasmonic oscillations. It is also known that if this frequency corresponds to that of the laser used for this type of measurement, then the structure used is suitable as a substrate for SERS technique.

In addition, the probability of the molecules being positioned at suitable distances directly depends on the number of hot spots. This increases the SERS enhancement factor. With regard to the application of sculptured thin films, the size of molecules studied also is of high importance. Therefore, in the design and production of this type of substrate one should consider all these factors.

Data availability The data of the results presented in this work are available from the authors of the paper.

Compliance with ethical standards

Conflict of interest The authors declare that they have no conflict of interest.

References

1. Raman, C.V., Krishnan, K.S.: A new type of secondary radiation. Nature **121**, 501 (1928)
2. Fleischmann, M., Hendra, P.J., McQuillan, A.J.: Raman spectra of pyridine adsorbed at a silver electrode. Chem. Phys. Lett. **26**(2), 163–166 (1974)
3. Fini, G.: Applications of Raman spectroscopy to pharmacy. J. Raman Spectrosc. **35**(5), 335–337 (2004)
4. Stetciura, I.Y., Markin, A.V., Bratashov, D.N., Sukhorukov, G.B., Gorin, D.A.: Nanoencapsulated and microencapsulated SERS platforms for biomedical analysis. Curr. Opin. Pharmacol. **18**, 149–158 (2014)
5. Edwards, H.G., Munshi, T., Anstis, M.: Raman spectroscopic characterisations and analytical discrimination between caffeine and demethylated analogues of pharmaceutical relevance. Spectrochim. Acta Part A Mol. Biomol. Spectrosc. **61**(7), 1453–1459 (2005)
6. Artyushenko, V., Schulte, F., Zabarylo, U., Berlien, H.-P., Usenov, I., Saeb Gilani, T., Eichler, H., Bogomolov, A., Krause, H., Minet, O.: Spectral fiber sensors for cancer diagnostics in vitro. In: European Conference on Biomedical Optics, Optical Society of America, p. 953720 (2015)
7. Liu, C.-H., Zhou, Y., Sun, Y., Li, J.Y., Zhou, L.X., Boydston-White, S., Masilamani, V., Zhu, K., Pu, Y., Alfano, R.R.: Resonance Raman and Raman spectroscopy for breast cancer detection. Technol. Cancer Res. Treat. **12**(4), 371–382 (2013)
8. Miloudi, L., Bonnier, F., Tfayli, A., Yvergnaux, F., Byrne, H.J., Chourpa, I., Munnier, E.: Confocal Raman spectroscopic imaging for in vitro monitoring of active ingredient penetration and distribution in reconstructed human epidermis model. J. Biophoton. **11**(4), 201700221 (2018)
9. Kong, K.V., Lam, Z., Goh, W.D., Leong, W.K., Olivo, M.: Metal carbonyl–gold nanoparticle conjugates for live-cell SERS imaging. Angew. Chem. Int. Ed. **51**(39), 9796–9799 (2012)
10. De Veij, M., Vandenabeele, P., Hall, K.A., Fernandez, F.M., Green, M.D., White, N.J., Dondorp, A.M., Newton, P.N., Moens, L.: Fast detection and identification of counterfeit antimalarial tablets by Raman spectroscopy. J. Raman Spectrosc. **38**(2), 181–187 (2007)
11. Wood, B.R., Bailo, E., AsghariKhiavi, M., Tilley, L., Deed, S., Deckert-Gaudig, T., McNaughton, D., Deckert, V.: Tip-enhanced Raman scattering (TERS) from hemozoin crystals within a sectioned erythrocyte. Nano Lett. **11**(5), 1868–1873 (2011)
12. Schmid, T., Sebesta, A., Stadler, J., Opilik, L., Balabin, R.M., Zenobi, R.: Tip-enhanced Raman spectroscopy and related techniques in studies of biological materials. Synth. Photon. Nanoscale Mater. VII **7586**, 758603 (2010)
13. Knauer, M., Ivleva, N.P., Niessner, R., Haisch, C.: A flow-through microarray cell for the online SERS detection of antibody-captured *E. coli* bacteria. Anal. Bioanal. Chem. **402**(8), 2663–2667 (2012)
14. Rull, F., Martinez-Frias, J., Medina, J.: Surface mineral analysis from two possible Martian analogs (Rio Tinto and Jaroso Ravine, Spain) using micro-, macro-, and remote laser Raman spectroscopy, European Geosciences Union. Geophys. Res. Abstr. **7**, 09114 (2005)
15. Wopenka, B., Pasteris, J.D.: Structural characterization of kerogens to granulite-facies graphite: applicability of Raman microprobe spectroscopy. Am. Mineral. **78**(5–6), 533–557 (1993)
16. Wilson, R., Monaghan, P., Bowden, S.A., Parnell, J., Cooper, J.M.: Surface-enhanced Raman signatures of pigmentation of cyanobacteria from within geological samples in a spectroscopic–microfluidic flow cell. Anal. Chem. **79**(18), 7036–7041 (2007)
17. Izake, E.L.: Forensic and homeland security applications of modern portable Raman spectroscopy. Forensic Sci. Int. **202**(1–3), 1–8 (2010)
18. Muehlethaler, C., Leona, M., Lombardi, J.R.: Review of surface enhanced Raman scattering applications in forensic science. Anal. Chem. **88**(1), 152–169 (2015)
19. Sägmüller, B., Schwarze, B., Brehm, G., Schneider, S.: Application of SERS spectroscopy to the identification of (3, 4-methylenedioxy) amphetamine in forensic samples utilizing matrix stabilized silver halides. Analyst **126**(11), 2066–2071 (2001)
20. Braz, A., López-López, M., García-Ruiz, C.: Raman spectroscopy for forensic analysis of inks in questioned documents. Forensic Sci. Int. **232**(1–3), 206–212 (2013)
21. Grand, J., de La Chapelle, M.L., Bijeon, J.-L., Adam, P.-M., Vial, A., Royer, P.: Role of localized surface plasmons in

surface-enhanced Raman scattering of shape-controlled metallic particles in regular arrays. Phys. Rev. B **72**(3), 033407 (2005)

22. Tsang, J., Kirtley, J., Bradley, J.: Surface-enhanced Raman spectroscopy and surface plasmons. Phys. Rev. Lett. **43**(11), 772 (1979)

23. Savaloni, H., Goli-Haghighi, S., Babaei, R.: Application of Mn–Cu helical star-shaped (pine tree-like) sculptured thin films with different symmetries using surface-enhanced raman spectroscopy (SERS). *Appl. Spectrosc.* p. 0003702819841913 (2019)

24. Efremov, E.V., Ariese, F., Mank, A.J.G., Gooijer, C.: Strong overtones and combination bands in ultraviolet resonance Raman spectroscopy. Anal. Chem. **78**(9), 3152–3157 (2006)

25. Kondepati, V.R., Oszinda, T., Heise, H.M., Luig, K., Mueller, R., Schroeder, O., Keese, M., Backhaus, J.: CH-overtone regions as diagnostic markers for near-infrared spectroscopic diagnosis of primary cancers in human pancreas and colorectal tissue. Anal. Bioanal. Chem. **387**(5), 1633 (2007)

26. Savaloni, H., Babaei, F., Song, S., Placido, F.: Characteristics of sculptured Cu thin films and their optical properties as a function of deposition rate. Appl. Surf. Sci. **255**, 8041–8047 (2009)

27. Tait, R.N., Smy, T., Brett, M.J.: Modelling and characterization of columnar growth in evaporated films. Thin Solid Films **226**, 196–201 (1993)

28. Eckertova, L.: Physics of Thin Films, 2nd edn. Plenum Press, Springer, Berlin (1986)

29. Siabi-Garjan, A.: Design and production and theoretical calculation of the optical and the electrical properties of sculptured thin films. Ph.D. thesis, University of Tehran (2014)

30. Savaloni, H., Haydari-Nasab, F., Abbas-Rohollahi, A.: Antibacterial effect, structural characterization, and some applications of silver chiral nano-flower sculptured thin films. J. Theor. Appl. Phys. **9**, 193–200 (2015)

31. Sengupta, A., Laucks, M.L., Davis, E.J.: Surface-enhanced Raman spectroscopy of bacteria and pollen. Appl. Spectrosc. **59**, 1016–1023 (2005)

32. Xia, Y., Xiong, Y., Lim, B.: Shape-controlled synthesis of metal nanocrystals: simple chemistry meets complex physics. Angew. Chem. Int. Ed. **48**, 60–103 (2009)

33. Atkins, P., De Paula, J.: Atkins' Physical Chemistry, p. 511. Oxford University Press, New York (2014)

34. Moskovits, M.: Surface enhanced spectroscopys. Rev. Mod. Phys. **57**, 783 (1985)

35. Le Ru, E.C., Blackie, E., Meyer, M., Etchegoin, P.G.: Surface enhanced Raman scattering enhancement factors: a comprehensive study. J. Phys. Chem. C **111**, 13794–13803 (2007)

36. Etchegoin, P., Le Ru, E.: Principle of Surface Enhanced Raman Spectroscopy. Elsevier, Amsterdam (2008)

37. Szabo, L., Herman, K., Mircescu, N.E., Falamas, A.: SERS and DFT investigation of 1-(2-pyridylazo)-2-naphthol and its metal complexes with Al(III), Mn(II), Fe(III), Cu(II), Zn(II) and Pb(II). Spectrochim. Acta A **93**, 266–273 (2012)

38. Savaloni, H., Babaei, R.: Surface enhanced Raman spectroscopy and structural characterization of Ag/Cu chiral nano-flower sculptured thin films. Appl. Surf. Sci. **280**, 439–445 (2013)

39. Boyd, S., Bertino, F., Ye, D., White, L.S., Seashols, S.J.: Highly sensitive detection of blood by surface enhanced Raman scattering. J. Forensic Sci. **58**, 753–756 (2013)

Publisher's Note Springer Nature remains neutral with regard to jurisdictional claims in published maps and institutional affiliations.